LETTERS
https://doi.org/10.1038/s41567-019-0750-y
nature physics

Spin–orbit-controlled metal–insulator transition in Sr_2IrO_4

B. Zwartsenberg[1,2], R. P. Day[1,2], E. Razzoli[1,2], M. Michiardi[1,2,3], N. Xu[4], M. Shi[4], J. D. Denlinger[5], G. Cao[6], S. Calder[7], K. Ueda[8], J. Bertinshaw[8], H. Takagi[8], B. J. Kim[9,10], I. S. Elfimov[1,2] and A. Damascelli[1,2]*

In the context of correlated insulators, where electron–electron interactions (*U*) drive the localization of charge carriers, the metal–insulator transition is described as either bandwidth- or filling-controlled[1]. Motivated by the challenge of the insulating phase in Sr_2IrO_4, a new class of correlated insulators has been proposed, in which spin–orbit coupling (SOC) is believed to renormalize the bandwidth of the half-filled $j_{\rm eff}$ = 1/2 doublet, allowing a modest *U* to induce a charge-localized phase[2,3]. Although this framework has been tacitly assumed, a thorough characterization of the ground state has been elusive[4,5]. Furthermore, direct evidence for the role of SOC in stabilizing the insulating state has not been established, because previous attempts at revealing the role of SOC[6,7] have been hindered by concurrently occurring changes to the filling[8–10]. We overcome this challenge by employing multiple substituents that introduce well-defined changes to the signatures of SOC and carrier concentration in the electronic structure, as well as a new methodology that allows us to monitor SOC directly. Specifically, we study $Sr_2Ir_{1-x}T_xO_4$ (T = Ru, Rh) by angle-resolved photoemission spectroscopy, combined with ab initio and supercell tight-binding calculations. This allows us to distinguish relativistic and filling effects, thereby establishing conclusively the central role of SOC in stabilizing the insulating state of Sr_2IrO_4. Most importantly, we estimate the critical value for SOC in this system to be $\lambda_c = 0.42 \pm 0.01$ eV, and provide the first demonstration of a spin–orbit-controlled metal–insulator transition.

The familiar tools of chemical doping and pressure have provided straightforward access to both a filling-controlled (FC) and bandwidth-controlled (BC) metal–insulator transition (MIT) in conventional correlated insulators. In an effort to unveil the role of spin–orbit coupling (SOC) in the insulating behaviour of Sr_2IrO_4, and whether it can indeed drive a MIT, we have attempted to controllably dilute SOC in the valence electronic structure by substituting Ir ($\lambda_{\rm SOC} \approx 0.4$ eV; refs. [11–13]) with Ru and Rh ($\lambda_{\rm SOC} \approx 0.19$ eV; refs. [14–16]). Although these substituents have similar values of $\lambda_{\rm SOC}$ and are both 4*d* ions with comparable values for *U* (refs. [17,18]) and ionic radii[19], they are otherwise distinct: Ru has one less electron than Rh, and is therefore associated with a markedly larger impurity potential. We will show through supercell tight-binding (TB) model calculations that this leads to a pronounced contrast in the consequences of Rh and Ru substitution: the larger impurity potential associated with Ru precludes a significant reduction of the valence SOC. By comparison, Rh is electronically more compatible with Ir, facilitating a successful dilution of SOC. We measure this evolution directly, through orbital mixing imbued by SOC, manifest experimentally in the photoemission dipole matrix elements. To comprehend all aspects of the MIT observed here for both Rh and Ru substitution, we consider individually the effects of filling (Fig. 1), correlations/bandwidth (Fig. 2) and SOC (Figs. 3 and 4), ultimately concluding that the transition in $Sr_2Ir_{1-x}T_xO_4$ is a spin–orbit-controlled MIT.

Having highlighted the three relevant aspects of the MIT, we begin our discussion by showcasing the changes both substituents introduce to the electronic structure of Sr_2IrO_4, as measured by angle-resolved photoemission spectroscopy (ARPES). Figure 1a–d summarizes ARPES spectra for $x = 0$; $x_{\rm Rh} = 0.22$; and $x_{\rm Ru} = 0.20$, 0.40. As reported previously[2], the pristine sample supports an energy gap, with a band maximum at X at a binding energy of around $E_{\rm b} = 0.25$ eV. When substituting Rh, a pseudo-gapped metallic state forms for concentrations $x \gtrsim 0.13$ (refs. [8–10]). This is exemplified by our $x_{\rm Rh} = 0.22$ data, shown in Fig. 1b,e. At comparable values of $x_{\rm Ru}$, the system remains insulating (see $x_{\rm Ru} = 0.20$ in Fig. 1d), and only when going as high as $x_{\rm Ru} = 0.40$ (Fig. 1c,f) do we find that the MIT has been traversed[20–22], consistent with transport measurements[21].

Within the metallic phase, the Fermi surface volume provides a direct measure of the hole doping introduced by the impurity atoms. We report a Brillouin zone coverage of 16% and 46% for Rh and Ru, respectively, corresponding to a nominal doping of 0.16 holes (at $x_{\rm Rh} = 0.22$) and 0.46 holes (at $x_{\rm Ru} = 0.40$), per formula unit. To within our level of certainty, each impurity atom then contributes approximately one hole carrier, with Ru perhaps contributing a somewhat larger number than Rh. This observation runs contrary to the expectations for a FC transition: despite contributing at least as many holes as Rh, the MIT critical concentration required for Ru is roughly double that of Rh. This precludes a transition described in terms of filling, despite earlier reports to the contrary[8–10]. An explanation in terms of the modification to the crystal structure upon Ru substitution can be equally excluded: the smaller ionic radius of Ru causes a minimal reduction of octahedral distortions (12° to 10°) up to the concentrations used in our study[21]. More importantly, such a reduction of distortions would increase the bandwidth[23], and the expected trend would be opposite to our observations.

---

[1] Quantum Matter Institute, University of British Columbia, Vancouver, BC, Canada. [2] Department of Physics and Astronomy, University of British Columbia, Vancouver, BC, Canada. [3] Max Planck Institute for Chemical Physics of Solids, Dresden, Germany. [4] Swiss Light Source, Paul Scherrer Institut, Villigen, Switzerland. [5] Advanced Light Source, Lawrence Berkeley National Laboratory, Berkeley, CA, USA. [6] Department of Physics, The Ohio State University, Columbus, OH, USA. [7] Neutron Scattering Division, Oak Ridge National Laboratory, Oak Ridge, TN, USA. [8] Max Planck Institute for Solid State Research, Stuttgart, Germany. [9] Department of Physics, Pohang University of Science and Technology, Pohang, South Korea. [10] Center for Artificial Low Dimensional Electronic Systems, Institute for Basic Science (IBS), Pohang, Republic of Korea. *e-mail: damascelli@physics.ubc.ca

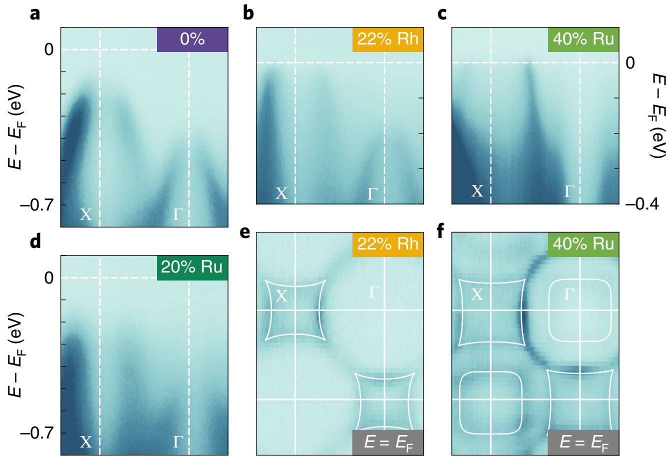

Fig. 1 | Dependence of the MIT on Rh and Ru substitution. a–d, Angle-resolved photoemission spectroscopy (ARPES) spectra along Γ–X for the pristine sample (**a**), $x_{Rh}=0.22$ (**a**), $x_{Ru}=0.40$ and $x_{Ru}=0.20$. **e**,**f**, Fermi surface maps for $x=0.22$ Rh and $x=0.40$ Ru. The sizes of the pockets are indicated with white lines. Fermi surface maps are integrated over 50 meV. All data are taken at $h\nu=64$ eV with temperatures between 120 K and 150 K for $x\leq0.10$, and below 40 K otherwise.

Alternatively, due to the presence of a sizable impurity potential for Ru (as discussed below), disorder effects could also be considered; however, recent studies regarding disorder in Mott systems point out that such effects would also push the critical concentration to lower values[22,24], precipitating once again an earlier onset of metallicity in the Ru-substituted compounds.

Looking beyond the disparate critical concentrations associated with Ru and Rh substitution, analysis of the ARPES spectral features allows for a more thorough comparison of these materials to be made. The selected energy distribution curves (EDCs) cut through the valence band maximum for each doping in Fig. 2a (Ru) and 2b (Rh), reflecting the evolution of each material across the MIT. This coincides with a definitive Fermi level crossing in the EDCs of Fig. 2a,b, from which we can infer the critical concentrations to be $x_{Rh}=0.13\pm0.03$ and $x_{Ru}=0.30\pm0.10$ (this matches previous photoemission work on the Rh-substituted compound[8–10]; as for the Ru-substituted samples, those have not previously been studied by photoemission). As the interpretation of EDC lineshape is non-trivial[25], we turn to an analysis of momentum distribution curves (MDCs) for a more quantitative analysis of the evolution of correlation effects. The MDC linewidth is directly related to the state lifetime and, by extension, to both electronic interactions and disorder[26–28]. Two representative MDCs are shown in Fig. 2c for $x_{Rh}=0.22$ and $x_{Ru}=0.40$. Widths from these, and other MDCs along the dispersion, are summarized in Fig. 2d. As can be inferred by a comparison of data from 20 K and 150 K, correlations—rather than thermal broadening—are the limiting factor in determining the MDC linewidth. Consideration of both $x_{Ru}=0.40$ and $x_{Rh}=0.22$ reveals remarkably similar interaction effects in the two compounds, despite their significant differences in composition and disorder. In addition, while spectral broadening at high binding energies precludes a precise evaluation of the bandwidth, we estimate the latter to be constant to within 10% over the range of Rh/Ru concentrations considered.

We have thus determined that while doping effects are comparable for Ru and Rh, similar correlated metallic phases are observed at very different concentrations. To rectify this apparent contradiction, one must consider the context of the present MIT: it has been proposed that the correlated insulating phase in Sr_2IrO_4 is stabilized by the strong SOC. This motivates consideration of the role SOC plays in the MIT for both Ru- and Rh-substituted compounds. The low-energy influence of SOC can be characterized by an effective value in the valence band, determined by the hybridization between atomic species as demonstrated in refs. [29,30]. This effect could cause a reduction of SOC effects in the valence band as a function of (Ru,Rh) substitution. We find the reduction of SOC to be strongly dependent on the presence of an impurity potential, which limits hybridization of host and impurity states, ultimately curtailing the dilution of SOC effects (see Supplementary Information). In light of the reported electronic phase separation for the Ru compound[31–33], this suggests that such dilution of SOC may be more effective for Rh, providing a natural explanation for their disparate critical concentration in substituted Sr_2IrO_4 compounds.

The model presented in the Supplementary Information to illustrate the mechanism of spin–orbit mixing can be made quantitative for the Ru/Rh iridates through consideration of impurity-substituted supercell models. Using density functional theory (DFT), at $x=0.25$ substitution, Fig. 3a shows good overlap between the Rh and Ir projected density of states (DOS). This can be compared against the same scenario for Ru in Fig. 3b, where the substituent DOS is found to align poorly with Ir. Such an offset, observed most clearly through consideration of the centre of mass of the Ru-projected DOS, has been reported previously for similar substitutions[34,35]. Calculating the band's centre of mass in terms of the projected densities of states for both, we find an impurity potential for Ru of 0.3 eV, which is close to the number found in refs. [34,35] (0.25 eV) and agrees with Wannier calculations (0.2 eV) performed on the same supercells. This establishes a reasonable starting point from which we can explore the influence of doping on SOC effects in more detail. This was carried out through the development of a supercell TB model. We expanded a single iridium TB Hamiltonian (see Supplementary Information) to a 64-site supercell, randomly substituting a fraction x of sites with an impurity atom. For the sake of simplicity, the impurities are assumed to differ from Ir in only their λ_{SOC} (0.19 eV for both Ru and Rh, 0.45 for Ir), and on-site potential (0.0 eV for Rh and Ir, 0.25 ± 0.05 eV for Ru). Similarly, octahedral distortions and electron correlations are neglected to better illustrate the energy shift of the j_{eff} states. We used the unfolding method[36–39] to project bands into the original Brillouin zone. By averaging the resulting spectral function over 200 random

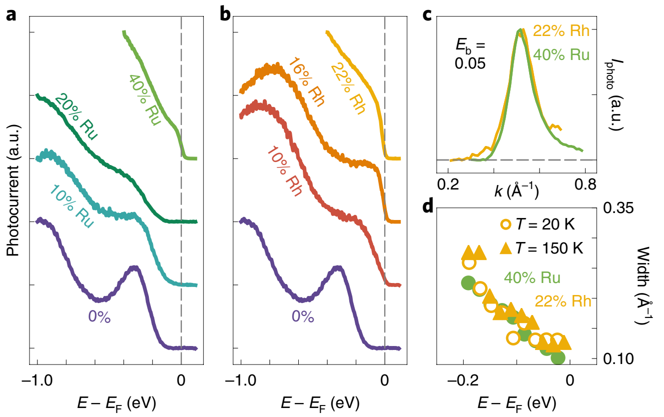

Fig. 2 | ARPES linewidth evolution with substitution. a,**b**, Energy distribution curves (EDCs) for Ru- (**a**) and Rh-substituted (**b**) samples, taken at the momentum with the leading edge closest to the Fermi energy. Photon energies and temperatures for the EDCs are the same as in Fig. 1. **c**, Momentum distribution curves (MDCs) for $x_{Ru}=0.40$ and $x_{Rh}=0.22$. **d**, MDC fits for $x_{Ru}=0.40$ and $x_{Rh}=0.22$. MDC data shown in **c** and **d** were taken using $h\nu=92$ eV at a temperature of 20 K.

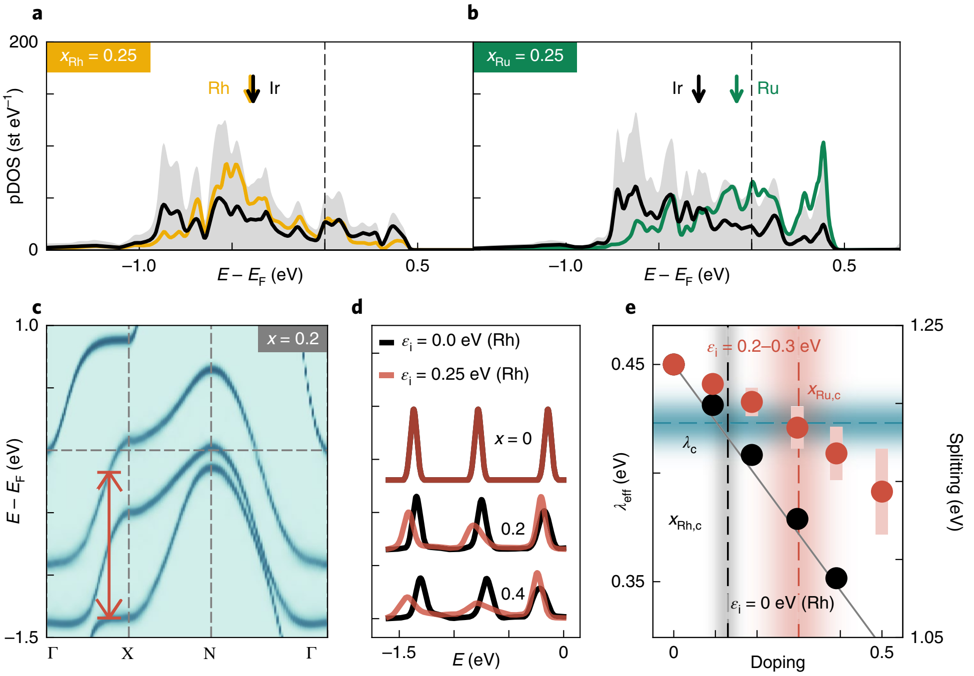

Fig. 3 | Reduction of SOC through supercell analysis. **a**,**b**, Plot of an analysis of the impurity potentials of Rh (**a**) and Ru (**b**) in Sr_2IrO_4, calculated by density functional theory. The grey background represents the total density of states (DOS), normalized by the number of transition metal (TM) sites. The black curves show the Ir projected DOS (pDOS) per Ir ion in the 25% substituted calculation in states per eV (st eV^{-1}), while the orange and green coloured curves reflect the pDOS per substituent ion for Rh and Ru, respectively. The arrows indicate the centre of mass for the projected bands. **c**, Supercell calculated spectrum for $x_{Rh} = 0.2$ obtained after unfolding. The effective splitting is indicated in red. **d**, Cuts (EDCs) for different concentrations of dopants at the position of the red arrow in **c** ($\mathbf{k}_{exp} = \left(\frac{3\pi}{4a}, 0\right)$). The substituted atoms have different SOC and on-site energy. We use $\lambda_{SOC} = 0.19$ eV and $\varepsilon_i = 0.0$ eV for Rh (black) and $\lambda_{SOC} = 0.19$ eV and $\varepsilon_i = 0.25$ eV for Ru (red). **e**, Progression of the splitting between the outermost peaks for simulations in **d** for Rh (black markers) and Ru (red markers). For Rh, a linear interpolation is plotted between the end members of the phase diagram. For Ru, the resulting range of splitting for $\varepsilon_i = 0.25 \pm 0.05$ is indicated by red shaded rectangles. The critical concentrations obtained from our measurements are indicated by the black (Rh) and red (Ru) vertical shaded areas. The blue shaded area indicates the inferred $\lambda_c = 0.42 \pm 0.01$.

configurations, we observe a smooth evolution of effective SOC in this system, which depends strongly on the impurity potential.

The results are summarized in Fig. 3, with a representative unfolded spectrum ($x_{Rh} = 0.20$) as plotted in Fig. 3c. We investigated the level spacing at $\mathbf{k}_{exp} = \left(\frac{3\pi}{4a}, 0\right)$, where a is the Ir–Ir distance, as indicated by the vertical arrow in Fig. 3c. This is the k-point at which we will later present experimental data. The change in splitting is seen clearly in Fig. 3d, where we plot a series of EDCs at $\mathbf{k}_{exp}$ for models with a non-zero on-site impurity potential (Ru, red) and for those without (Rh, black). This doping dependence is summarized in Fig. 3e. The right vertical axis reflects the splitting observed at $\mathbf{k}_{exp}$, and the left the value of λ_{SOC} that would produce the corresponding splitting in a model without substitutions (that is, for an overall uniform value of λ_{SOC}). This second axis serves to illustrate the effective SOC caused by substitution of Ir with Rh and Ru. From the progression in Fig. 3e it is evident that Rh should dilute SOC more efficiently than Ru: the black markers trace the interpolation between the values of Ir and Rh, indicated by the grey line. Meanwhile, the modelled impurity potential for Ru (0.25 ± 0.05 eV) prevents successful dilution of SOC. The results in Fig. 3e suggest that the different critical concentrations for the two substituents can be attributed to a common parameter: a value for SOC of $\lambda_c \approx 0.42 \pm 0.01$ (blue shaded area, Fig. 3e) yields critical concentrations ($x_{Rh} \approx 0.15$ and $x_{Ru} \approx 0.3$) that fit well with our experimental observations. The theoretical results presented in ref. [40] suggest that SOC in Sr_2IrO_4 is only marginally above the threshold for the insulating state, and that such a small change could drive the transition. The dilution of SOC is therefore found to provide a compelling theoretical picture of the transition.

Having demonstrated this evolution of SOC via substitution and its ability to provide a natural explanation for the transition in $Sr_2Ir_{1-x}T_xO_4$, we aimed to substantiate these predictions experimentally. To establish a convenient metric for SOC, we leveraged the symmetry constraints of the photoemission matrix element. Dipole selection rules allow transitions from only certain orbitals: because d_{xz} (d_{yz}, d_{xy}) is even (odd) in the experimental scattering plane, states composed of this cubic harmonic are only observable with π (σ) polarization. As SOC mixes these orbitals into linear combinations prescribed by the j_{eff} construction[2], we quantified SOC by comparing the ratio of even/odd states at strategically chosen points in the Brillouin zone where these symmetry-based selection rules are most well defined. In the absence of SOC, the state along Γ–X_x (defined in Fig. 4) in Sr_2IrO_4 would be of pure d_{xz} character: any photoemission from this state using σ polarization must be due to the admixture of d_{yz} and d_{xy} introduced by SOC. More quantitatively, of interest here is the value of M_x^σ, the matrix element at the X_x point, which we normalize in our results through division by M_y^σ. A simulation of this quantity based on an ab initio TB model for Sr_2IrO_4 with variable SOC is shown as a black solid line in Fig. 4e. The model takes into account the effects of experimental geometry as well as photon energy and polarization (for further details see Supplementary Information). The curve shows a clear decrease of M_x^σ/M_y^σ as a function of SOC, demonstrating the possibility for a direct measure of λ_{SOC} via ARPES.

Motivated by the supercell calculations, we investigated the progression of M_x^σ/M_y^σ experimentally in a series of Rh- and Ru-substituted samples. In Fig. 4a–d we plot constant energy contours for each of the concentrations, recorded with σ-polarized

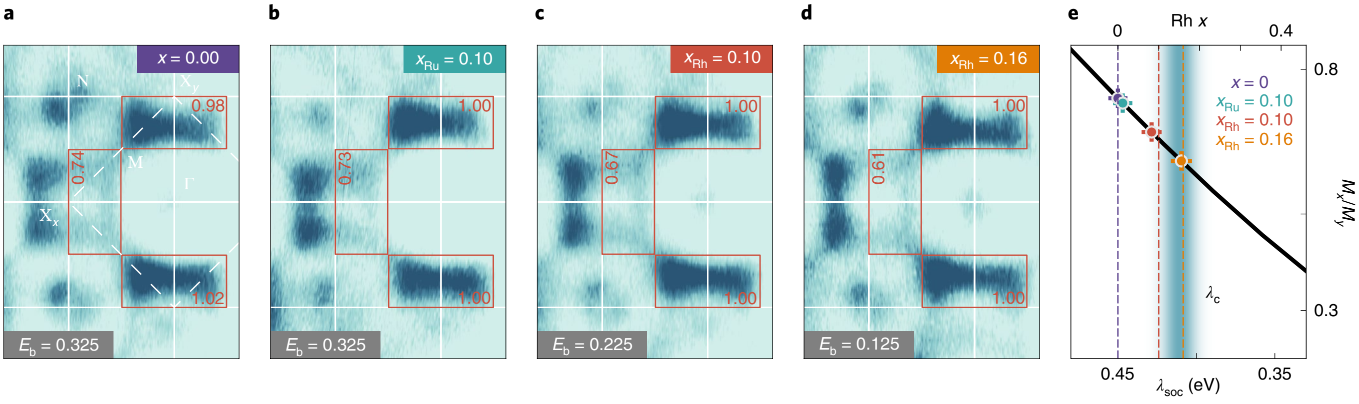

Fig. 4 | Observation of the reduction of SOC via the ARPES dipole matrix element. a–d, Constant energy maps for different concentrations of x_{Rh}, using σ-polarized light: $x = 0.00$ (**a**), $x_{Ru} = 0.10$ (**b**), $x_{Rh} = 0.10$ (**c**), $x_{Rh} = 0.16$ (**d**). The constant energy maps are integrated over 150 meV to improve the numerical accuracy, and taken at an energy such that the size of the pocket around X is the same for all concentrations. The relevant states used for the analysis are indicated using the red boxes, and their integrated values are shown within. All data are taken at 64 eV, with temperatures at 120 K for $x = 0.00$ and $x_{Ru} = 0.10$, 70 K for $x_{Rh} = 0.10$ and 20 K for $x_{Rh} = 0.16$, all chosen to mitigate the effects of charging. **e**, The calculated ratio of matrix elements for a model of Sr_2IrO_4 (for details see Supplementary Information), plotted as a function of SOC (black curve). The coloured markers indicate the ratio of the experimental values shown in **a**–**d**. Error bars are calculated from the standard deviation over the integrated range in energy. The top axis in **e** indicates the substitution required to produce the SOC value on the bottom axis, predicted by the supercell calculations in Fig. 3e. The dashed lines indicate the expected effective SOC from the nominal concentrations of the Rh-substituted samples.

light. To compare the different samples, we consider constant energy maps at the energy that places the state of interest at $\mathbf{k}_{\mathrm{exp}} = \left(\frac{3\pi}{4a}, 0\right)$. Integrating and dividing the ARPES intensity within the indicated regions of Fig. 4a–d yields the ratio M_x^σ / M_y^σ. We can proceed to make a quantitative connection with an effective SOC strength by plotting the experimental data points alongside the simulated curve in Fig. 4e. The latter has been normalized to the experimental data for pristine Sr_2IrO_4, allowing for an effective λ_{SOC} strength to be extracted for the Rh/Ru-substituted samples. This analysis yields λ_{SOC} values of 0.443 ($x_{\mathrm{Ru}} = 0.10$), 0.424 ($x_{\mathrm{Rh}} = 0.10$) and 0.408 eV ($x_{\mathrm{Rh}} = 0.16$). A connection to the supercell calculations can be made through these λ_{SOC} values: the associated impurity concentrations in Fig. 3e agree remarkably well with the actual experimental values, made explicit in the case of Rh with the top horizontal axis of Fig. 4e. This confirms the premise of our supercell model and the sensitivity to the impurity potential for successful dilution of λ_{SOC}. In connection to the MIT, the $\lambda_c = 0.42 \pm 0.01$ eV at $x_{\mathrm{Rh}} = 0.15$ obtained from Fig. 3e is overlaid in Fig. 4e. Generally speaking, λ_c can also be a function of filling, U, bandwidth and disorder, among others. SOC thus represents but a single axis within a higher-dimensional phase space. As filling, distortions and disorder are expected to expedite rather than suppress the MIT in Ru-substituted samples[21–24], the rate in dilution of SOC emerges as the primary factor responsible for the dichotomy in x_c observed for Ru and Rh. This indicates the critical role of SOC in the MIT of $Sr_2Ir_{1-x}T_xO_4$ for both Rh and Ru substitution.

The combination of SOC-sensitive techniques and the comparison of Ru- and Rh-substituted samples place us in a unique position to comment on the role of SOC in the MIT of Sr_2IrO_4, demonstrating a SOC-controlled collapse of a correlated insulating phase. By doing so, as an important corollary to these results, our work conclusively establishes Sr_2IrO_4 as a relativistic Mott insulator. Additionally, we note that the investigation into mixing SOC discussed in Supplementary Fig. 3 was calculated for a generic two-site Hamiltonian. As such, this mechanism pertains to other systems in which this type of physics appears, such as SOC tuning in $Ga_{1-x}Bi_xAs$ (ref. [41]) and topological insulators[42–46]. Moreover, the sensitivity of these phenomena to an impurity potential has implications for ongoing efforts to enhance SOC effects in graphene and related systems through adatom deposition and other proximity-related techniques[29,30,47–49].

Online content

Any methods, additional references, Nature Research reporting summaries, source data, extended data, supplementary information, acknowledgements, peer review information; details of author contributions and competing interests; and statements of data and code availability are available at https://doi.org/10.1038/s41567-019-0750-y.

Received: 21 March 2019; Accepted: 13 November 2019;
Published online: 27 January 2020

References

1. Imada, M., Fujimori, A. & Tokura, Y. Metal–insulator transitions. *Rev. Mod. Phys.* **70**, 1039 (1998).
2. Kim, B. J. et al. Novel J_{eff}=1/2 Mott state induced by relativistic spin–orbit coupling in Sr_2IrO_4. *Phys. Rev. Lett.* **101**, 076402 (2008).
3. Kim, B. J. et al. Phase-sensitive observation of a spin–orbital Mott state in Sr_2IrO_4. *Science* **323**, 1329–1332 (2009).
4. MorettiSala, M., Boseggia, S., McMorrow, D. F. & Monaco, G. Resonant X-ray scattering and the j_{eff}=1/2 electronic ground state in iridate perovskites. *Phys. Rev. Lett.* **112**, 026403 (2014).
5. Kim, B. J. & Khaliullin, G. Resonant inelastic X-ray scattering operators for t_{2g} orbital systems. *Phys. Rev. B* **96**, 085108 (2017).
6. Qi, T. F. et al. Spin–orbit tuned metal–insulator transitions in single-crystal $Sr_2Ir_{1-x}Rh_xO_4$ ($0 \le x \le 1$). *Phys. Rev. B* **86**, 125105 (2012).
7. Lee, J. S., Krockenberger, Y., Takahashi, K. S., Kawasaki, M. & Tokura, Y. Insulator–metal transition driven by change of doping and spin–orbit interaction in Sr_2IrO_4. *Phys. Rev. B* **85**, 035101 (2012).
8. Brouet, V. et al. Transfer of spectral weight across the gap of Sr_2IrO_{4ind} induced by La doping. *Phys. Rev. B* **92**, 081117 (2015).
9. Cao, Y. et al. Hallmarks of the Mott-metal crossover in the hole-doped pseudospin-1/2 Mott insulator Sr_2IrO_4. *Nat. Commun.* **7**, 11367 (2016).
10. Louat, A. et al. Formation of an incoherent metallic state in Rh-doped Sr_2IrO_4. *Phys. Rev. B* **97**, 161109 (2018).
11. Mattheiss, L. F. Electronic structure of RuO_2, OsO_2 and IrO_2. *Phys. Rev. B* **13**, 2433–2450 (1976).
12. Moon, S. J. et al. Dimensionality-controlled insulator–metal transition and correlated metallic state in 5 *d* transition metal oxides $Sr_{n+1}Ir_nO_{3n+1}$ ($n = 1$, 2 and ∞). *Phys. Rev. Lett.* **101**, 226402 (2008).

13. Kim, B. H., Khaliullin, G. & Min, B. I. Magnetic couplings, optical spectra and spin–orbit exciton in 5*d* electron Mott insulator Sr_2IrO_4. *Phys. Rev. Lett.* **109**, 167205 (2012).
14. Haverkort, M. W., Elfimov, I. S., Tjeng, L. H., Sawatzky, G. A. & Damascelli, A. Strong spin–orbit coupling effects on the Fermi surface of Sr_2RuO_4 and Sr_2RhO_4. *Phys. Rev. Lett.* **101**, 026406 (2008).
15. Veenstra, C. N. et al. Spin–orbital entanglement and the breakdown of singlets and triplets in Sr_2RuO_4 revealed by spin- and angle-resolved photoemission spectroscopy. *Phys. Rev. Lett.* **112**, 127002 (2014).
16. Earnshaw, A., Figgis, B. N., Lewis, J. & Peacock, R. D. The magnetic properties of some d^4-complexes. *J. Chem. Soc.* **0**, 3132 (1961).
17. Mravlje, J. et al. Coherence–incoherence crossover and the mass-renormalization puzzles in Sr_2RuO_4. *Phys. Rev. Lett.* **106**, 096401 (2011).
18. Martins, C., Aichhorn, M., Vaugier, L. & Biermann, S. Reduced effective spin–orbital degeneracy and spin–orbital ordering in paramagnetic transition-metal oxides: Sr_2IrO_4 versus Sr_2RhO_4. *Phys. Rev. Lett.* **107**, 266404 (2011).
19. Shannon, R. D. Revised effective ionic radii and systematic studies of interatomic distances in halides and chalcogenides. *Acta Crystallogr. A* **32**, 751–767 (1976).
20. Cava, R. J. et al. Localized-to-itinerant electron transition in $Sr_2Ir_{1-x}Ru_xO_4$. *Phys. Rev. B* **49**, 11890 (1994).
21. Yuan, S. J. et al. From $J_{\mathrm{eff}}=1/2$ insulator to $J_{\mathrm{eff}}=1/2$ -wave superconductor in single-crystal $J_{\mathrm{eff}}=1/2$. *Phys. Rev. B* **92**, 245103 (2015).
22. Wang, Z. et al. Disorder induced power-law gaps in an insulator–metal Mott transition. *Proc. Natl Acad. Sci. USA* **115**, 11198 (2018).
23. Martins, C. *Interplay of Spin–Orbit Coupling and Electronic Coulomb Interactions in Strontium Iridate Sr_2IrO_4*. Thesis, Ecole Polytechnique X (2010).
24. Heidarian, D. & Trivedi, N. Inhomogeneous metallic phase in a disordered Mott insulator in two dimensions. *Phys. Rev. Lett.* **93**, 126401 (2004).
25. Kaminski, A. et al. Renormalization of spectral line shape and dispersion below T_c in $Bi_2Sr_2CaCu_2O_{8+\delta}$. *Phys. Rev. Lett.* **86**, 1070–1073 (2001).
26. Damascelli, A. Probing the electronic structure of complex systems by ARPES. *Phys. Scr.* **T109**, 61 (2004).
27. Hufner, S. *Photoelectron Spectroscopy: Principles and Applications* (Springer, 1995).
28. Mahan, G. D. in *Electron and Ion Spectroscopy of Solids* (ed. Fiermans, L.) Ch. 1, 1–53 (Plenum Press, 1978).
29. Weeks, C., Hu, J., Alicea, J., Franz, M. & Wu, R. Engineering a robust quantum spin Hall state in graphene via adatom deposition. *Phys. Rev. X* **1**, 021001 (2011).
30. Hu, J., Alicea, J., Wu, R. & Franz, M. Giant topological insulator gap in graphene with 5*d* adatoms. *Phys. Rev. Lett.* **109**, 266801 (2012).
31. Carter, S. A. et al. Mechanism for the metal–insulator transition in $Sr_2Ir_{1-x}Ru_xO_4$. *Phys. Rev. B* **51**, 17184–17187 (1995).
32. Glamazda, A. et al. Effects of hole doping on magnetic and lattice excitations in $Sr_2Ir_{1-x}Ru_xO_4$ ($x=0$–0.2). *Phys. Rev. B* **89**, 104406 (2014).
33. Calder, S. et al. Strong anisotropy within a Heisenberg model in the $J_{\mathrm{eff}}=1/2$ insulating state of $Sr_2Ir_{0.8}Ru_{0.2}O_4$. *Phys. Rev. B* **94**, 220407 (2016).
34. Wadati, H., Elfimov, I. & Sawatzky, G. A. Where are the extra *d* electrons in transition-metal-substituted iron pnictides? *Phys. Rev. Lett.* **105**, 157004 (2010).
35. Levy, G. et al. Probing the role of Co substitution in the electronic structure of iron pnictides. *Phys. Rev. Lett.* **109**, 077001 (2012).
36. Boykin, T. B. & Klimeck, G. Practical application of zone-folding concepts in tight-binding calculations. *Phys. Rev. B* **71**, 115215 (2005).
37. Ku, W., Berlijn, T. & Lee, C. C. Unfolding first-principles band structures. *Phys. Rev. Lett.* **104**, 216401 (2010).
38. Haverkort, M. W., Elfimov, I. S. & Sawatzky, G. A. Electronic structure and self energies of randomly substituted solids using density functional theory and model calculations. Preprint at https://arxiv.org/abs/1109.4036 (2011).
39. Popescu, V. & Zunger, A. Extracting E versus $\vec{k}$ E effective band structure from supercell calculations on alloys and impurities. *Phys. Rev. B* **85**, 085201 (2012).
40. Watanabe, H., Shirakawa, T. & Yunoki, S. Microscopic study of a spin–orbit-induced Mott insulator in Ir oxides. *Phys. Rev. Lett.* **105**, 216410 (2010).
41. Fluegel, B. et al. Giant spin–orbit bowing in $GaAs_{1-x}Bi_x$. *Phys. Rev. Lett.* **97**, 067205 (2006).
42. Xu, S.-Y. et al. Topological phase transition and texture inversion in a tunable topological insulator. *Science* **332**, 560–564 (2011).
43. Sato, T. et al. Unexpected mass acquisition of dirac fermions at the quantum phase transition of a topological insulator. *Nat. Phys* **7**, 840 (2011).
44. Brahlek, M. et al. Topological-metal to band-insulator transition in $(Bi_{1-x}In_x)_2Se_3$ thin films. *Phys. Rev. Lett.* **109**, 186403 (2012).
45. Wu, L. et al. A sudden collapse in the transport lifetime across the topological phase transition in $(Bi_{1-x}In_x)_2Se_3$. *Nat. Phys.* **9**, 410 (2013).
46. Vobornik, I. et al. Observation of distinct bulk and surface chemical environments in a topological insulator under magnetic doping. *J. Phys. Chem. C* **118**, 12333–12339 (2014).
47. Avsar, A. et al. Spin–orbit proximity effect in graphene. *Nat. Commun.* **5**, 4875 (2014).
48. Straßer, C. et al. Long- versus short-range scattering in doped epitaxial graphene. *Nano Lett.* **15**, 2825–2829 (2015).
49. Barker, B. A. et al. Geometry and electronic structure of iridium adsorbed on graphene. *Phys. Rev. B* **99**, 075431 (2019).

Methods

Single crystals of $Sr_2Ir_{1-x}Rh_xO_4$ were grown with nominal concentrations of $x_{Rh} = 0.0, 0.10, 0.16, 0.22$ and measured with electron probe microanalysis to be within 0.01 of their nominal concentration. Crystals of $Sr_2Ir_{1-x}Rh_xO_4$ were grown with nominal concentrations of $x_{Ru} = 0.10, 0.20, 0.40$. Measurements were carried out at the SIS beamline at the Swiss Lightsource (Rh-substituted samples) and at the Merlin beamline at the Advanced Lightsource (Rh- and Ru-substituted samples). All measurements were performed on freshly cleaved surfaces, where the pressure during measurement and cleavage was always lower than 3.3×10^{-10} mbar. Measurements used for inference of spin–orbit coupling values were performed with 64 eV photons, using light polarized perpendicular to the analyser slit direction (σ polarization). The rotation axis of the manipulator for acquisition of the Fermi surface was parallel to the slit direction. The sample was mounted such that the Ir–O bonds (Γ–X) were aligned to this axis of rotation. Temperatures were chosen to be as low as possible while mitigating the effects of charging and are reported in the figure captions. A tight-binding model was constructed from a Wannier orbital calculation using the Wannier90 package[50]. The Wannier90 calculations were performed on results from DFT calculations done with the Wien2k package[51,52]. Supercell and matrix element calculations were performed using the chinook package[53]. Further details are provided in the Supplementary Information. The DOS calculations presented in Fig. 3 were performed with the Wien2k package. The supercell configuration assumed a single layer with eight TM ions per unit cell. The presented results at $x = 0.25$ are similar to those found for $x = 0.125$ and $x = 0.5$.

Data availability

The data represented in Figs. 2 and 3 are available as source data in Supplementary Data 2 and 3. All other data that support the plots within this paper and other findings of this study are available from the corresponding author upon reasonable request.

References

50. Mostofi, A. A. et al. An updated version of Wannier90: a tool for obtaining maximally-localised Wannier functions. *Comput. Phys. Commun.* **185**, 2309–2310 (2014).
51. Blaha, P. et al. *WIEN2k, An Augmented Plane Wave + Local Orbitals Program for Calculating Crystal Properties* (Karlheinz Schwarz, Techn. Universität Wien, 2018).
52. Kuneš, J. et al. Wien2wannier: from linearized augmented plane waves to maximally localized Wannier functions. *Comput. Phys. Commun.* **181**, 1888–1895 (2010).
53. Day, R. P., Zwartsenberg, B., Elfimov, I. S. & Damascelli, A. Computational framework chinook for angle-resolved photoemission spectroscopy. *Npj Quantum Mater.* **4**, 54 (2019).

Acknowledgements

We thank A. Nocera, M. Franz and G.A. Sawatzky for critical reading of the manuscript and useful discussions. This research was undertaken thanks in part to funding from the Max Planck-UBC-UTokyo Centre for Quantum Materials and the Canada First Research Excellence Fund, Quantum Materials and Future Technologies Program. The work at UBC was supported by the Killam, Alfred P. Sloan and Natural Sciences and Engineering Research Council of Canada's (NSERC's) Steacie Memorial Fellowships (A.D.), the Alexander von Humboldt Fellowship (A.D.), the Canada Research Chairs Program (A.D.), NSERC, Canada Foundation for Innovation (CFI) and the CIFAR Quantum Materials Program. E.R. acknowledges support from the Swiss National Science Foundation (SNSF, grant no. P300P2_164649). B.J.K. was supported by IBS - R014-A2.

Author contributions

B.Z. and A.D. conceived the experiment. B.Z., E.R. and M.M. collected the experimental data. N.X., M.S. and J.D.D. provided experimental support. G.C., S.C., K.U., J.B., H.T. and B.J.K. grew the single crystals. B.Z. and R.P.D. performed data analysis. B.Z. performed simulations, with input from R.P.D., I.S.E. and A.D. B.Z., R.P.D. and A.D. wrote the manuscript, with input from all authors. I.S.E. and A.D. supervised the project. A.D. was responsible for overall project direction, planning and management.

Competing interests

The authors declare no competing interests.

Additional information

Supplementary information is available for this paper at https://doi.org/10.1038/s41567-019-0750-y.

Correspondence and requests for materials should be addressed to A.D.

Reprints and permissions information is available at www.nature.com/reprints.

Peer Review Information *Nature Physics* thanks Fahad Mahmood and the other, anonymous, reviewer(s) for their contribution to the peer review of this work.